EES Catalysis

Check for updates

Plasmonic gold nanostars conjugated poly(heptazine imide) for photocatalytic H₂O₂ production from O₂ reduction†

Pankaj Sharma, [ID] *[a] Koen Evers,[a] Maicon Delarmelina, [ID] [b] Anton Y. Bykov,[c] Martin Wilding,[d] Tianhao He,[a] Anatoly V. Zayats, [ID] [c] Richard A. Catlow [ID] [bde] and Fang Xie [ID] *[a]

Recent advances in photocatalytic systems for H₂O₂ production have led to improvements in both efficiency and selectivity; however, the practical application of current photocatalysts remains limited by low H₂O₂ production rates, poor long-term stability, and challenges in scalability. In this study, we present a novel photocatalyst based on the integration of gold nanostars (AuNSs) into poly(heptazine imide) (PHI) resulting in a system that is highly efficient for H₂O₂ production. The resulting AuNSs–PHI catalyst achieved a remarkable H₂O₂ generation rate of 286.95 mM g⁻¹ h⁻¹ under solar irradiation, utilising O₂ reduction coupled with isopropanol oxidation. This enhanced performance is primarily attributed to localized surface plasmon resonance (LSPR) effects from the embedded gold nanostars, which significantly boost light absorption and charge separation efficiency. The critical role of the optimized nanostructure was further validated through time-dependent density functional theory (TDDFT) calculations on a gold cluster (Au₂₀) adsorbed onto PHI, providing theoretical insight into the observed experimental H₂O₂ production enhancement. These findings demonstrate the potential of plasmon-enhanced photocatalysis as a viable pathway for sustainable and scalable H₂O₂ production.

Broader context

Hydrogen peroxide, one of the 100 most important chemical substances globally, is widely used in modern industries and is considered a promising energy carrier. However, the predominant production method, anthraquinone oxidation, is neither economical nor sustainable due to its complex, energy-intensive process and significant environmental impact. This limitation necessitates the development of safer, greener, and more efficient alternatives. Photocatalytic H₂O₂ production has emerged as a promising alternative, offering a sustainable approach by utilizing sunlight, water, and air. However, its low production rate currently limits industrial applications. In this study, a novel plasmonic-enhanced photocatalysis strategy is proposed, integrating plasmonic gold nanostars with the highly photoactive molecular catalyst poly(heptazine imide). This strategy enhances efficiency by increasing metal/semiconductor interfacial areas and improving charge separation, thereby overcoming key challenges in photocatalytic processes. The resulting hybrid catalyst achieves superior H₂O₂ production under mild conditions, utilising sunlight, water, air, and organic waste. This innovation not only advances the efficiency of photocatalytic H₂O₂ production but also provides a scalable, environmentally friendly pathway to sustainable chemical synthesis.

Introduction

Hydrogen peroxide (H₂O₂) is a multifunctional compound with significant applications across various industries, including sustainable energy storage, water purification, and green chemical synthesis.[1] Its relevance is further underscored in processes such as fuel generation, bleaching, rocket propulsion, and environmental remediation.[2–4] However, current production methods face critical limitations. The conventional anthraquinone process is undesirable from both an environmental and economic point of view,[5] and the direct catalytic synthesis of H₂O₂ from H₂ and O₂[6,7] presents substantial challenges for large-scale implementation due to inherent safety risks, particularly the explosive nature of the H₂–O₂ gas mixture.[8,9] In contrast, sunlight-driven production of H₂O₂ from water and oxygen has

[a] Department of Materials, Imperial College London, London SW7 2AZ, UK.
E-mail: sharmapankaj47@gmail.com, f.xie@imperial.ac.uk
[b] School of Chemistry, Cardiff University, Cardiff CF10 3AT, UK
[c] Department of Physics, Kings College London, WC2R 2LS, UK
[d] UK Catalysis Hub, Research Complex at Harwell, OX11 0FA, UK
[e] Department of Chemistry, University College London, London WC1 0AJ, UK
† Electronic supplementary information (ESI) available. See DOI: https://doi.org/10.1039/d5ey00216h

emerged as a promising alternative, addressing both the sustainability and safety challenges by eliminating the need for H_2 and reducing carbon emissions.[9–12] Recent advances in photocatalyst design and reaction pathways have demonstrated substantial progress in this area, particularly in enhancing reaction efficiencies and selectivity.[13–17] Despite these notable advancements, several challenges persist (such as suboptimal H_2O_2 production rates, limited photocatalyst stability, and scalability issues) hindering the practical application of photocatalytic H_2O_2 production technology.[18–20]

On the other hand, recent studies have shown that incorporating plasmonic nanoparticles (PNPs), including Al,[21,22] Cu,[23] Ag,[24] and Au,[25] into photocatalytic systems extends their operational wavelength range beyond the UV spectrum and enhances solar energy utilization due to localized surface plasmon resonance (LSPR) and surface plasmon polaritons (SPPs).[26–28] Additionally, PNPs facilitate hot electron generation, which minimizes recombination losses and serves as an electron reservoir for efficient charge utilization.[29] Leveraging the advantages of PNPs, we strategically designed a plasmonic metal incorporated molecular photocatalyst to achieve more efficient and scalable H_2O_2 production.

Here, we report the successful incorporation of plasmonic gold nanostars (AuNSs) into one of the most efficient molecular photocatalysts, poly(heptazine imide) (PHI). Regarding the techno-economic feasibility, while noble metals like Au are costly, the actual loading used in our system is extremely low (≤ 0.6 wt%), and the enhancement in efficiency may offset the material cost in practical applications. We also highlight recent advances in Au recovery and recycling could further improve economic feasibility. Overall, we consider AuNSs–PHI a viable strategy for scalable H_2O_2 production. As a first step, we synthesized hierarchical three-dimensional (3D) thin nanoflakes of the PHI photocatalyst, which produced a record high H_2O_2 production rate of 161 mM g^{-1} h^{-1}. We found that interlayer intercalation and surface embellishment with alkali metals, the introduction of specific $-C\equiv N$ groups and surface defects contributed to the high H_2O_2 yield. To investigate the effect of PNPs on photocatalytic H_2O_2 production, we next grew plasmonic AuNSs onto the 3D-nanoflakes of PHI, synthesizing AuNSs-conjugated PHI (AuNSs–PHI) photocatalyst (Fig. 1a). The results demonstrated that AuNSs–PHI exhibits significantly higher photocatalytic activity (H_2O_2 generation rate of 286.95 mM g^{-1} h^{-1}) than PHI. To gain further insight, we used density functional theory (DFT) calculations for both PHI and AuNSs–PHI to analyse the charge density distribution across different crystal planes and explore the impact of AuNSs incorporation on the photoactivity of PHI. Moreover, we proposed an innovative and sustainable approach to reuse organic waste from laboratories to produce green energy carriers. This advancement represents a significant step toward the practical implementation of sustainable green chemical production technology.

Results and discussion

Progression of the reaction pathway and the evolution of nanoflake morphology of PHI

Following our previously reported modified method, PHI-structured carbon nitride (CN) was synthesized through direct ionothermal polymerisation of urea.[12] The synthesis was carried out in the presence of a eutectic KCl/LiCl salt mixture at 550 °C under a continuous flow of argon gas within a tube furnace. In parallel, tri-s-triazine structured CN (TST) was synthesized through thermal polymerization. This parallel synthesis enabled a comparative study between these two CN catalysts for application in the solar-driven O_2 reduction reaction (SORR). Understanding the reaction pathway for PHI formation is crucial as it directly influences the catalyst's efficiency, stability, and overall performance. A detailed investigation of this pathway allows for optimization of the synthesis process, leading to the development of highly efficient, stable, and cost-effective photocatalysts. To elucidate the reaction pathway and monitor the morphological evolution during synthesis, we performed four distinct series of ionothermal polymerization experiments. Detailed conditions for each series are summarized in Table S1, ESI.† The resulting samples were subsequently subjected to comprehensive advanced characterization techniques (Fig. S1–S3, and Table S2, ESI†). Fig. 1b and c depict the reaction pathway and morphological evolution of PHI during the ionothermal polymerization process, respectively.

Fig. S1a, ESI† displays the XRD patterns of PHI obtained at various temperatures during the ionothermal polymerization of urea. At a polymerization temperature of 300 °C (PHI300 °C), distinct sharp peaks are observed corresponding to the crystalline intermediate melamine phase,[30] N-(2,8-diamino-4-imino-4H-[1,3,5]triazino[1,2-a][1,3,5]triazin-6-yl) cyanamide, and melem adduct phase.[31] As the polymerization temperature increases to 400 °C (PHI400 °C), these sharp peaks transition into a broad peak at 27.3° and a minor peak at 42.7°, indicating a transformation from highly crystalline to relatively amorphous material. At a polymerization temperature of 550 °C (PHI), the XRD pattern shows seven distinct broad peaks at 8.46°, 12.2°, 14.6°, 21.8°, 28.2°, 35.74°, and 43.76° corresponding to (−110), (010), (−210), (−320), (001), (−530), and (42−1) planes of PHI structured CN, respectively.[32] Among these, the peaks at 28.2° and 8.46° are strong and sharp while the others are weak and broad. The intense diffraction peak at 28.2° is attributed to the polymeric layered structure of PHI with interlayer stacking of the conjugated aromatic segment, resembling a graphite-like layered structure.

Fourier transform infrared spectroscopy (FTIR) has also been employed to track the progression of the PHI polymerisation reaction by monitoring alterations in the characteristic peaks associated with both the precursor and the developing polymeric structure. The FTIR spectra (Fig. S1b, ESI†) provide crucial insights into the emergence and disappearance of functional groups, such as amino (–NH), cyano (–CN), and imine groups, throughout the polymerization process. The FTIR spectrum for
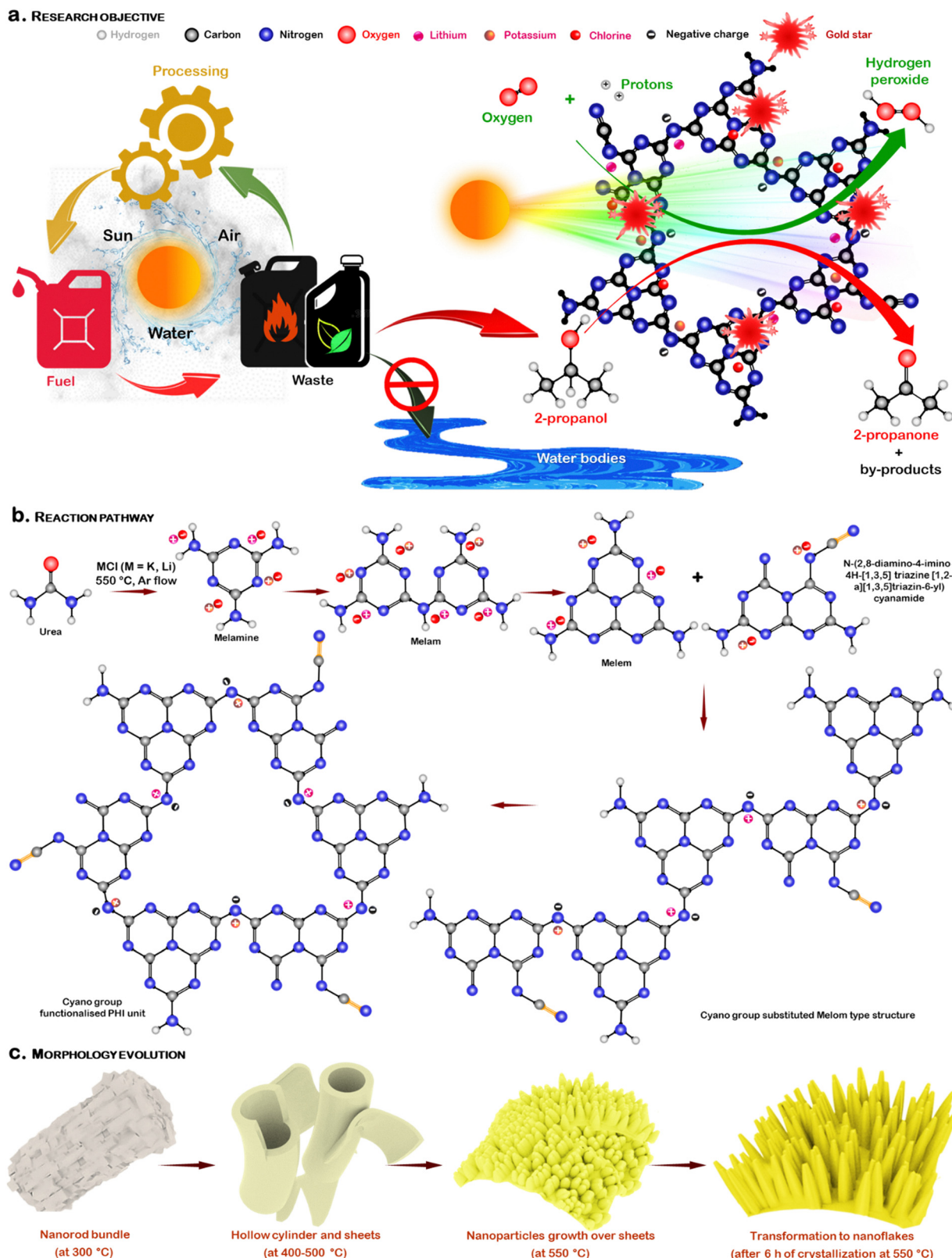
Fig. 1 Greener route of H_2O_2 production and reaction pathway of PHI formation. (a) Schematic illustration of the greener route of H_2O_2 production and the reaction on AuNSs−PHI. (b) The potential intermediate stages, and the growth mechanism of ionothermally polymerized PHI photocatalyst. (c) The progression of PHI 3D nanoflakes begins with the formation of bundled morphology particles resembling peculiar 3D nanorods, achieved through the heating of precursors at 300 °C.

$PHI_{300\,°C}$ aligns with XRD results (Fig. S1a $PHI_{300\,°C}$, ESI†), further confirming the presence of melamine, N-(2,8-diamino-4-imino-4H-[1,3,5]triazino[1,2-a][1,3,5]triazin-6-yl) cyanamide, and melem adduct phase as reaction intermediates.[31,33] In the FTIR spectrum of $PHI_{300\,°C}$, distinctive broad bands in the spectral range of 3000–3400 cm^{-1} signify symmetric and antisymmetric stretch vibrations of N···H hydrogen bonds, N–H (residual or terminal –NH$_2$ group), and O–H (–OH group) bonds. Conversely, these vibrational bands are nearly absent in the corresponding FTIR spectrum of samples collected at higher polymerization temperatures (Fig. S1b $PHI_{400\,°C}$–$PHI_{550\,°C}$, ESI†).[34] Notably, bands around 800 and 1570 cm^{-1} corresponding to breathing modes of triazine units and aromatic CN heterocycles, respectively[35,36] become more defined with increasing polymerization temperature. The spectra have been labelled for comparative analysis (Fig. S1b, ESI†). The appearance of bands around 992, 1143, and 1375 cm^{-1} (highlighted by a pink colour block) confirmed the substitution of the terminal –NH$_2$ by –OH groups, resulting in surface –OH group grafting (–C–OH) upon intercalation of K, Li, and Cl elements. Moreover, these vibrational peaks serve as indicators of the presence of alkali metal cations in the PHI structure. The stretching peak for the cyano group (–C≡N) at 2177 cm^{-1} with shoulder peaks indicates surface functionalization due to structural defects persisting after polymerization at 400 °C. The –C≡N group in PHI imparts a robust electron-withdrawing property to attract electrons from electron donors, facilitating enhanced separation of charge carriers and improved photochemical properties.[37,38] The formation of –C≡N results from the interaction of –OH with the amine groups within the heptazine rings during high-temperature ionothermal polymerization.[39,40] Additionally, the reduction in amino content observed during polymerization is also linked to the functionalization of the PHI framework through –C≡N groups. The FTIR spectra (Fig. S1b, ESI†) validated the evolving framework of PHI with the elevation of polymerization temperature.

To comprehend the stability and phase alterations in the synthesized PHI-structured CN samples, thermal analysis was conducted using thermogravimetric-differential scanning calorimetry (TG-DSC). The TG-DSC thermograms for the $PHI_{300\,°C}$ sample (Fig. S1c and d, ESI†) distinctly reveal multiple phase transformations in this intermediate specimen. The abrupt weight loss within the 250–400 °C range signifies simultaneous sublimation and thermal condensation of intermediate melamine and melem. A consistent reduction in weight between 420 and 650 °C corresponds to deamination and material decomposition. Further weight decrease is ascribed to material disappearance through the generation of nitrogen and cyano fragments. The $PHI_{400\,°C}$, partially functionalized with cyano groups (–C≡N) (Fig. S1b, ESI†), not only demonstrates enhanced stability (Fig. S1c and d, ESI†) compared to $PHI_{300\,°C}$ but also suggests the potential adsorption of gases and water vapour. The thermal stability and phase transformation profiles of $PHI_{500\,°C}$, $PHI_{550\,°C}$, and PHI are nearly identical, except for the weight loss associated with degassing. This is attributed to improved surface functionality and the complete polymerization of urea into the PHI

framework. Notably, these samples exhibit instability when subjected to temperatures exceeding 650 °C and heating up to 900 °C resulting in no observable material residue.

Ultraviolet-visible diffuse reflectance spectroscopy (UV-DRS) was used to track alterations in the optical attributes of potential intermediates throughout the PHI growth (Fig. S2a, and b, ESI†), offering valuable insights into its structural evolution. The negative absorption observed in the UV range, particularly for $PHI_{300\,°C}$ and $PHI_{400\,°C}$ samples, can be attributed to the stronger adsorption of the BaSiO$_4$ reference used for spectrophotometer calibration. The spectrum for $PHI_{300\,°C}$ reveals absorption peaks in the UV region, indicating electronic transitions involving the absorption of higher-energy photons. Analysis of the electronic absorption properties of dried $PHI_{300\,°C}$ shows three optical absorption edges at 266, 304, and 361 nm (Fig. S2a, ESI†), emphasizing the presence of melamine, melam, N-(2,8-diamino-4-imino-4H-[1,3,5]triazino[1,2-a][1,3,5]triazin-6-yl) cyanamide, and melem in the adduction phase. The positions of these absorption edges offer insights into the energy levels and electronic transitions within these intermediate molecules.[41] As the colour of PHI samples collected at different temperatures shifted from off-white to greenish-yellow (inset optical images Fig. S2a, ESI†), a noticeable redshift in the absorption band edge within the range of 260–480 nm was observed, indicating the progression of the polymerization reaction and PHI growth. This redshift may be attributed to the increase in polymerization degree, π-plane conjugation, and delocalized aromatic π-conjugation. Moreover, the absorption spectra highlight an increase in light absorption intensity with increasing polymerization temperature and time, reflecting improved optical properties of the materials. From the Kubelka–Munk plots (Fig. S2b, ESI†), it can be observed that the band gap energy of PHI samples collected at 300, 400, 500, and 550 °C was estimated to be approximately 3.68 eV ($PHI_{300\,°C}$), 2.89 eV ($PHI_{400\,°C}$), 2.76 eV ($PHI_{500\,°C}$), and 2.65 eV ($PHI_{550\,°C}$), respectively, suggesting the band gap decrease with increasing polymerization temperature. In summary, the results obtained from XRD, FTIR, TG-DSC and UV-DRS characterisation and analyses identified potential reaction intermediates involved in PHI synthesis and confirmed the reaction pathway for PHI synthesis, as illustrated in Fig. 1b.

The morphology in PHI is crucial as it influences surface area, charge separation, light absorption, and reactivity. Customizing the morphology of PHI is imperative to optimize its photocatalytic efficiency for SORR. Therefore, SEM micrographs were captured at various magnifications and areas for samples obtained at different growth stages (Fig. S3, ESI†). The SEM micrographs indicate a distinct mechanism governing the growth of 3D PHI nanoflakes (Fig. 1c). Following the initial mixture of precursors and liquefaction around 160 °C, a visible solid product ($PHI_{300\,°C}$) was obtained at 300 °C. SEM images of the $PHI_{300\,°C}$ sample (Fig. S3 $PHI_{300\,°C}$, ESI†) illustrate that the polymerized urea, in the presence of a eutectic mixture of KCl and LiCl, adopted a morphology characterized by a self-assembled bundle of nanorods. The dimensions of the individual primary nanorods/nanoparticles ranged from 5 to 20 nm in diameter and exhibited lengths exceeding 600 nm. The

potential factor contributing to the aggregation, self-assembly, and ordering of primary intermediate particles is attributed to the incorporation of alkali halides. The cations within the synthesis system are deemed to play a crucial role in the ordering process. The SEM image (Fig. S3 PHI$_{300\,°C}$, ESI†) indicates that a significant proportion of the PHI$_{300\,°C}$ samples comprise bundles of nanorods, with isolated nanoparticles and nanorods present in close proximity. As the polymerization reaction proceeded, the bundles of nanorods transitioned into sheets and smooth surfaced hollow cylinders at 400 °C (PHI$_{400\,°C}$) (Fig. S3 PHI$_{400\,°C}$, ESI†). Subsequently, the sheets were further folded into smaller diameter cylinders, and the larger diameter cylinders obtained at 400 °C underwent a transformative deformation process, turning into sheets at 500 °C (PHI$_{500\,°C}$) (Fig. S3 PHI$_{500\,°C}$, ESI†). The SEM image presented in Fig. S3 PHI$_{500\,°C}$, ESI† clearly illustrates the deformation of the cylinders into sheets. Therefore, under the synthesis conditions, an increase in polymerization temperature leads to the disintegration of large cylinders into layered polymers, followed by folding into cylinder structures, manifesting as a repetitive process. Within the same sample (PHI$_{500\,°C}$), we also observed the nucleation of small nanoparticles as elucidated in the last image of Fig. S3 PHI$_{500\,°C}$, ESI.† At a polymerization temperature of 550 °C (PHI$_{550\,°C}$), we observed the emergence of nanoparticles from both sheet and cylinder surfaces (Fig. S3 PHI$_{550\,°C}$, ESI†) as illustrated in the growth mechanism depicted in Fig. 1c. Upon close examination of the SEM images (Fig. S3 PHI, ESI†) acquired after 6 hours of polymerization at 550 °C, it becomes evident that the nanoparticles grown on the surface undergo a transformation into PHI nanoflakes.

After determining the reaction pathway for PHI synthesis and the evolution of its morphology, computational studies were employed to assess the effect of PHI's chemical structure I, which incorporates cyano groups and metal cations, along with an examination of its optoelectronic properties. All calculations were performed using long-range corrected hybrid DFT functional CAM-B3LYP[42] together with LANL2DZ and 6-31G(d,p) basis set for Au and lighter atoms (C, N, and H), respectively. Excited states were calculated using standard Tamm–Dancoff approximation[43–45] as implemented in Orca 5.0.3.[46] Six heptazine units were used to construct representative models of PHI, which included the defect-free structure (**1**), as well as amino methyl cyanamide and cyanomide terminated structures (**2b** and **3**, Fig. 2a). We note that larger band gaps and shorter wavelengths are expected for the model systems due to their reduced size when compared to the experimental one. The calculated absorption spectra for these structures exhibited one high-intensity band around 250 nm (Fig. S4, ESI†). This absorption band in system **1** is mainly formed by two single electron excitations at 251.9 nm with comparatively symmetrical charge density distribution, resulting in accumulation of hole density over the π and non-bonding orbitals of N, and electron density over π*-type orbitals of C atoms (Fig. 2b). The defective heptazine moiety resulted in additional single electron excitations around 250 nm, including now high hole density localisation over terminal cyano groups, as well as over

other surrounding N atoms (**3**, Fig. 2b). A complete comparison of selected excited states and corresponding hole and electron density distribution is given in Table S3, ESI.† The effect of H$^+$/K$^+$ cation exchange was also considered for investigating the deprotonation of linking amine groups. The most stable systems (**4a**, **5b**, and **6b**) are shown in Fig. 2a. Other less stable alternative structures are described in Fig. S5, ESI.† Deprotonation of the linking NH group and interaction with K$^+$ cation resulted in the appearance of a new absorption band at higher wavelengths (∼295 nm, Fig. S6, ESI†) with associated hole/electron density localization occurring exclusively within the heptazine moieties linked by the deprotonated N atom (**4a** and **6b**, Fig. 2b). The computed redshift is consistent with the formation of new energy states above the VB and the reduction of band gap energies (Fig. S7 and Table S4, ESI†). These results confirm the key role of cyano groups present in PHI in the charge separation and hole localization process during photochemical reactions. Additionally, they show the band-shifting effect of electron excitations due to H$^+$/K$^+$ cation exchange in PHI.

To investigate further the textural properties and validate the mesoporous nature observed in the PHI samples through SEM analysis (Fig. S9–S13, ESI†), N$_2$ adsorption–desorption measurements were conducted at 77 K. The textural parameters of these photocatalysts, derived from N$_2$ adsorption–desorption isotherms, are compiled in Table S2, ESI.† The pore size distribution curves, indicative of a mesoporous structure, display a broad distribution of pores primarily arising from the interparticle spacing resulting from the ordered alignment of nanoparticles. The porous character, stemming from the distinctive nanoflake morphology, could potentially enhance light-harvesting efficiency.

Plasmonic AuNSs decorated poly(heptazine imide) (AuNSs–PHI) photocatalyst synthesis

To introduce a plasmonic component to PHI, spherical plasmonic gold nanoparticles were used as 'seed' Au$_{Seed}$ (Fig. S8, ESI†), to create plasmonic gold nanostars AuNSs (Fig. S10, ESI†). We then decorated PHI nanoflakes with 0.3 wt% Gold nanostars, creating AuNSs–PHI through a freeze drying method described in the ESI.†

AuNSs exhibit a broad and strong absorption band in the visible-NIR region, with a characteristic tail extending beyond 800 nm (Fig. S22, ESI†). This optical signature is well-known for anisotropic AUNSs and is indicative of the dipole and multi-polar LSPR modes arising from their branched morphology. (Spherical Au nanoparticles in comparison show a narrower plasmon peak around ∼520 nm.) The superior performance of AuNSs–PHI, compared to either PHI alone or PHI loaded with spherical Au particles (*e.g.*, Au$_{Seed}$@PHI, Fig. S36, ESI†), as well as size-dependent performance differences (Fig. 8d) indirectly confirm the critical role of the localized surface plasmon resonance (LSPR) effect of the optimized AuNSs, to enhance photocatalytic activity. The LSPR effect facilitates both the generation and injection of plasmonic hot electrons into PHI,
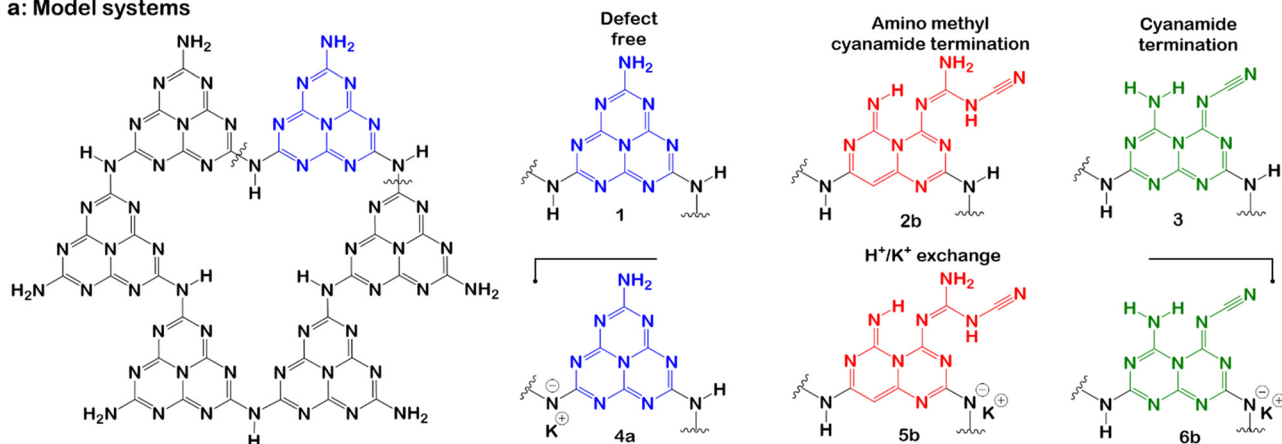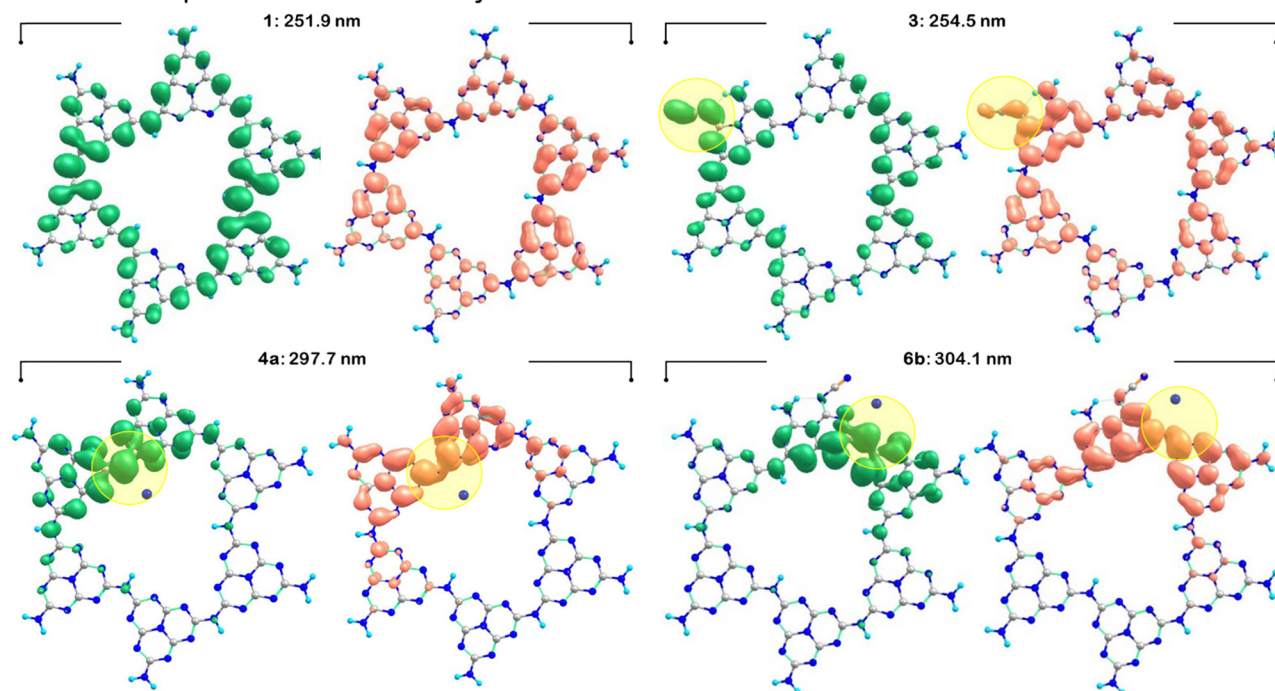
Fig. 2 Model systems of PHI and TDDFT calculations. (a) Model systems used to investigate the structural effect over the absorption properties of PHI. Defect free (**1**), as well as amino methyl cyanamide (**2b**) and cyanamide terminated structures (**3**) were considered. For linking amine groups, H^+/K^+ exchange was also investigated (**4–6**). (b) Selected examples of hole (green)/electron (pink) density distribution over **1**, **3**, **4a**, **6b** structures. Yellow circles highlight terminal cyano and deprotonated amine sites. Grey, blue, white, and purple spheres indicate carbon, nitrogen, hydrogen, and potassium atoms, respectively.

as well as improved light absorption and local electromagnetic field enhancement.

To determine the effective incorporation of AuNSs onto PHI nanoflakes and highlight the structural variances among AuNSs–PHI, TST, and PHI, the powder X-ray diffraction (PXRD) patterns are shown in Fig. S17, ESI† and Fig. 3a. The diffraction peaks at 13.15° and 27.6° in the XRD pattern for TST corresponded to lattice planes (100) and (002) of tri-*s*-triazine structured g-C_3N_4, respectively. Notably, the absence of the (100) lattice plane peak in the XRD pattern of PHI (Fig. 3a) suggests the occurrence of nitrogen defects, such as $-C \equiv N$, leading to a shift in the long-range in-plane and out-of-plane structural

order. Therefore, the introduction of alkali metals and halide ions through intercalation confirms potential alterations in interplanar stacking. This possibly leads to adjustments in the electron-rich π-conjugated framework, in-plane lattice packing, and the creation of edge defects, resulting in functionalization with cyano groups ($-C \equiv N$) and $-NO_x$ groups.[47] Additionally, the (002) planar diffraction peak of TST at 27.61° exhibits a shift to a higher angle of 28.21° in PHI (elaborated schematic details are provided in Fig. S17, ESI†), indicating a reduction in the distance of interplanar stacking within the polymeric layers. In the XRD pattern of AuNSs–PHI (Fig. 3a), the additional diffraction peaks at 38.2°, 44.3°, and 64.7° correspond to (111), (200), and (220)
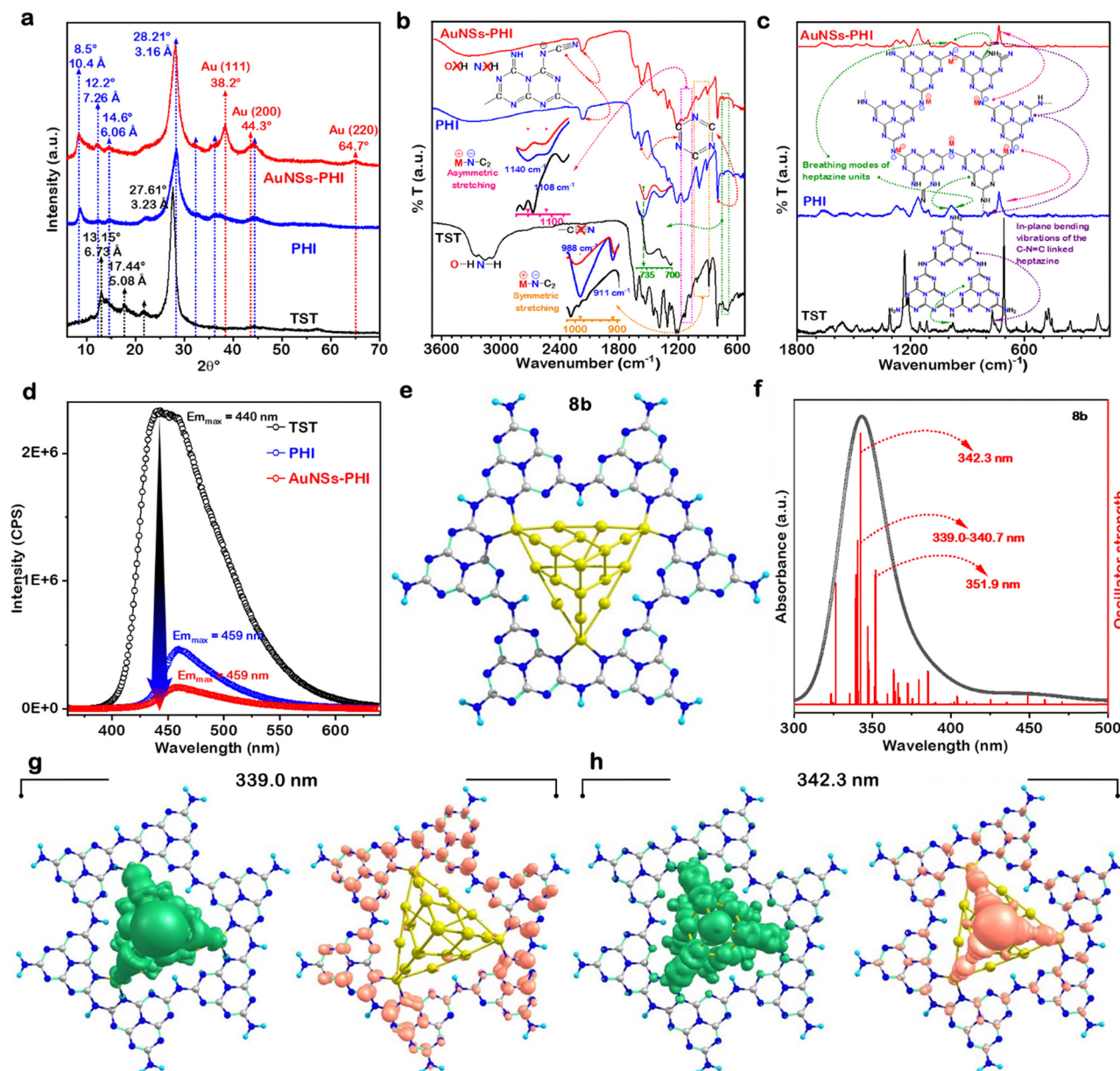
Fig. 3 Structural analysis of AuNSs−PHI relative to TST and PHI and TDDFT calculations. (a) XRD patterns, (b) ATR-FTIR spectra, (c) Raman spectra, and (d) PL spectra of TST, PHI, and AuNSs−PHI. (e) Most stable anchoring mode for Au$_{20}$ → 1 interaction (structure **8b**). (f) Computed absorption spectrum for **8b**. (g) and (h) Selected examples of electron excitation and hole (green)/electron (pink) density distribution. Grey, blue, white, and yellow spheres indicate carbon, nitrogen, hydrogen, and gold atoms, respectively.

lattice planes of Au nanostars, respectively, confirming the successful loading of Au nanostars onto PHI nanoflakes.

Vibrational spectroscopic techniques, specifically Fourier transform infrared (FTIR) and Raman spectroscopy, were employed for the analysis of chemical structure and surface functionality. These FTIR (Fig. 3b, and Fig. S18, ESI†) and Raman (Fig. 3c) spectra are in very good agreement with those reported in the literature.[48,49] Additionally, these techniques were applied to compare the structural characteristics of photocatalysts (TST and PHI) and the plasmonic photocatalyst. The FTIR spectrum presented in Fig. 3b, as well as the segmented Fig. S18, ESI,† show vibrational peaks with each peak precisely

indexed. Inset images in the spectra highlight each peak to facilitate clear differentiation among these samples. Raman spectroscopy further successfully identified specific fingerprint IR-inactive vibration modes, prominently capturing the heptazine unit's breathing modes at 734 and 985 cm^{-1}. Moreover, the analysis revealed a distinctive peak at 769 cm^{-1}, attributed to the in-plane bending vibration of the C–N=C linked heptazine in the TST sample, while a noteworthy shift of this peak to higher wave numbers was observed in PHI and AuNSs–PHI samples, as shown in Fig. 3c.[50,51]

To evaluate the photocatalytic activity and gain insights into the separation and recombination dynamics of photogenerated

charge carriers, the photoluminescence emission spectra were recorded during excitation at three different wavelengths (300, 350, and 400 nm) for TST, PHI, and AuNSs–PHI (Fig. 3d and Fig. S19, ESI†). TST displayed a pronounced, high-intensity broad emission spectrum, peaking at 440 nm (bandgap ∼430 nm) for all three excitation wavelengths, indicating a higher recombination rate of photogenerated charge carriers. In contrast, PHI exhibited a notable reduction in peak intensity at 459 nm (bandgap ∼465 nm), indicative of a suppressed electron–hole pair recombination rate and improved charge carrier separation efficiency. Consequently, the PHI photocatalyst effectively hinders various radiative charge carriers' recombination pathways due to a cyano group functionalised aromatic-structured PHI. Furthermore, the photoluminescence emission of AuNSs–PHI was significantly quenched, exhibiting a featureless emission profile. This observation suggests that the introduction of plasmonic AuNSs onto PHI expedites the separation of photogenerated charges. It is noteworthy that for TST, the PL emission peak is located near the bandgap energy, whereas TST spectrum is broader. These results suggest that PHI and AuNSs–PHI contain fewer mid-gap states, which are typically associated with non-radiative recombination processes. As band-to-band recombination is primarily radiative, the suppression of defect-mediated pathways implies an overall reduction in non-radiative recombination. The LSPR in Au nanostars facilitates hot electron generation, enabling the nanostars to act as electron acceptors and suppress electron–hole recombination. While the existence of other plasmonic characteristics remains uncertain in this study (Fig. S21, ESI†), the spectrum of AuNSs with extinction maxima at ∼800 nm (Fig. S22, ESI†) suggests the injection of hot electrons into the conduction band of PHI, leaving hot holes in their sp bands. These hot holes can either combine with the electrons of PHI or directly participate in oxidation reactions. This bidirectional transfer of charge carriers contributes to the overall enhancement in the photocatalytic activity of AuNSs–PHI by reducing the charge recombination rate.

This hypothesis was verified by TDDFT calculations for model system **8**. Structures **8** (Table S5, ESI†) were constructed by the absorption of the gold cluster containing 20 atoms (Au$_{20}$) over structure **1**. This gold cluster presents a tetragonal geometry for modelling the interaction between experimental gold nanostars and PHI. Fourteen alternative anchoring modes were identified between **1** and Au$_{20}$ (Table S5, ESI†), and the most stable structure (**8b**) is illustrated in Fig. 3e. In this case, Au$_{20}$ presents three of its corners anchored between inner aromatic N atoms of neighbouring heptazine moieties. Reduction of the band gap was computed for **8b** in comparison to **1** (ΔE_{BG} = −0.592 eV, Table S4, ESI†) due to the formation of Au s-type band above the VB of **1** (Fig. S30, ESI†). As a result, the main absorption band computed for these systems was red-shifted by ∼100 nm in comparison to **1**. Two main types of charge separation were identified within the main absorption band: hole density localized over the s- and d-type orbitals of the gold cluster and electron density localized at π*-type orbitals over C atoms of heptazine units (Fig. 3g); additionally, charge

separation within the gold cluster was computed for slightly higher wavelengths (Fig. 3h). The former demonstrates the possibility of electrons for the VB of gold being injected into the CB of PHI, reducing charge recombination and increasing photocatalytic activity. A complete analysis of selected electron excitations is given in Fig. S24 and Table S6, ESI†.

To assess the charge separation and transport characteristics at the interface of the samples (AuNSs–PHI, PHI, and TST), electrochemical impedance spectroscopy (EIS) measurements were conducted under both light irradiation and dark conditions. As anticipated, the Nyquist plot for AuNSs–PHI (Fig. 4a) displayed a significantly smaller arc radius compared to PHI and TST, indicating that AuNSs–PHI has inherently lower resistance for charge-carrier transport than the TST. EIS results also suggest that TST exhibits a greater difference under illumination *versus* dark conditions compared to PHI and AuNSs–PHI. This smaller difference for PHI and AuNSs–PHI indicates fewer deep trap states in these materials, which is consistent with their lower resistance in the dark relative to TST. These findings further support the conclusion that PHI demonstrates superior charge separation efficiency compared to TST, and AuNSs–PHI exhibiting an even higher degree of charge separation than PHI. The structurally modulated, –C≡N functionalised, and alkali-metal-impregnated heptazine imide core not only modulates light absorption towards longer wavelengths (discussed later in Fig. 4d) but also suppresses radiative charge recombination, resulting in fast interfacial charge transfer and effective separation of photogenerated electron–hole pairs in AuNSs–PHI. Additionally, the photocurrent density-potential profiles illustrated in Fig. 4b show the photoelectrochemical (PEC) performance of AuNSs–PHI, PHI, and TST photoanodes for water oxidation. These results highlight the remarkably enhanced photocurrent response of AuNSs–PHI, indicating the promoted dissociation and transport processes of the photoinduced charge carriers. The PEC performance findings complement the photoluminescence (Fig. 3d) and EIS (Fig. 4a) results, indicating a reduction in the recombination of electron–hole pairs and a decrease in impedance on AuNSs–PHI photoelectrode.

Additionally, a systematic investigation was conducted on the optical properties and electronic band structure of AuNSs–PHI with a comparative analysis of TST and PHI. The remarkable light absorption efficiency of PHI and AuNSs–PHI is substantiated through UV-DRS, as depicted in Fig. 4c. In comparison with TST, AuNSs–PHI exhibited elevated light absorption, spanning both the UV and visible regions, accompanied by a distinct red-shift and an extended tail with an absorption peak around 800 nm (Fig. 4c and Fig. S22, ESI†). This spectral behaviour is attributed to the presence of loaded plasmonic Au nanostars. The red shift observed in the absorption spectrum of AuNSs–PHI implies an extension of π-conjugation and the existence of a delocalized aromatic π-conjugated system. The visual inspection of digital images (Fig. S32, ESI†) revealed a discernible colour transition from white (TST) to greenish-yellow (PHI), and finally to dark green upon loading with Au nanostars (AuNSs–PHI). The heightened light absorption efficiency of
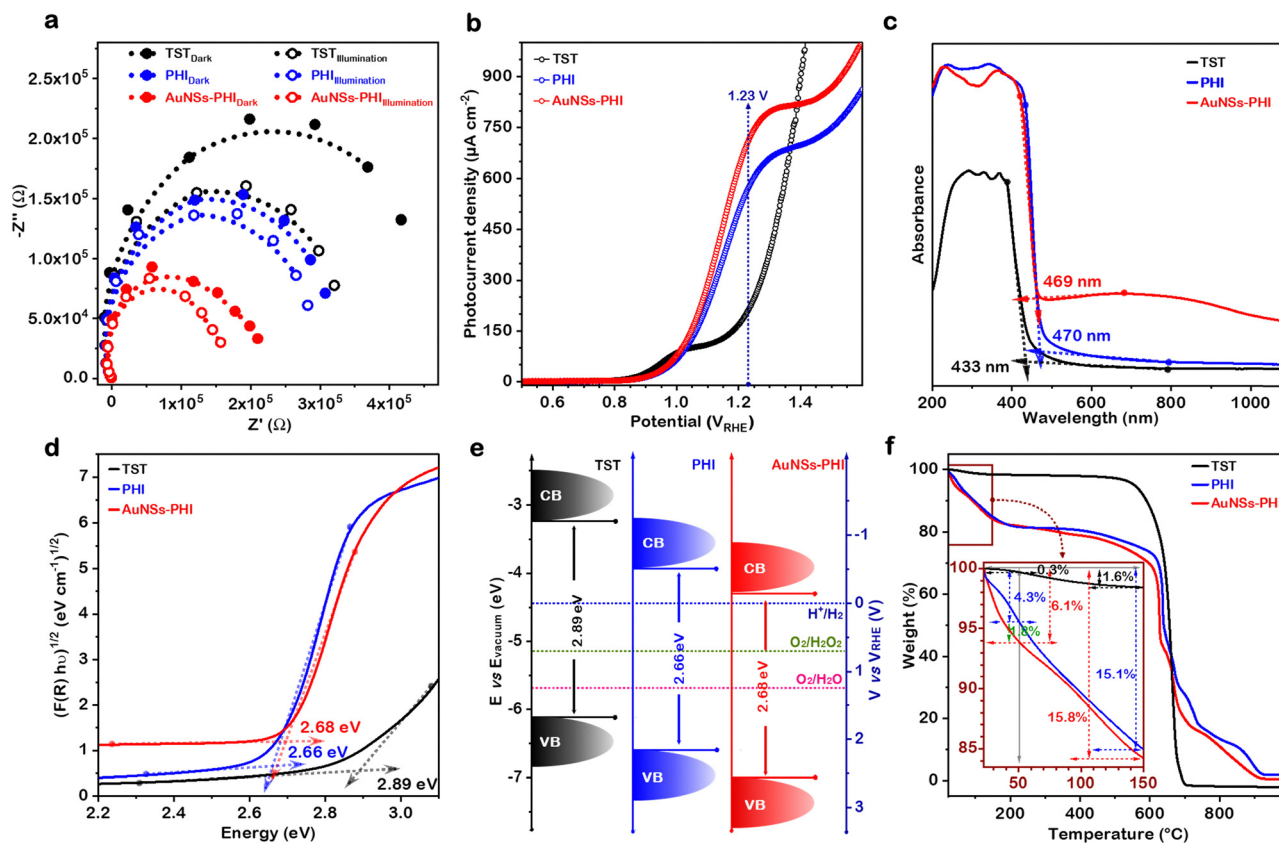
Fig. 4 Photo-electrochemical and thermogravimetric analysis of AuNSs−PHI relative to TST and PHI. (a) EIS Nyquist plots in the dark and under illumination, and (b) photocurrent density-potential profile of TST, PHI, and AuNSs−PHI. (c) UV-vis absorbance spectra highlighting the improvement in light absorbance relative to tri-s-triazine-structured g-C₃N₄ (TST). (d) Tauc plots for the bandgap calculations. (e) Schematic of band gap and energy level bands with respect to vacuum level and reversible hydrogen electrode (RHE). (f) TGA thermograms for TST, PHI and AuNSs−PHI.

AuNSs–PHI is likely attributed to the occurrence of multiple diffuse reflectance within the 3D nanoflake architecture, facilitating the trapping and deep penetration of solar radiation.

The Tauc plots presented in Fig. 4d were used to calculate the band gap energies (E_{BG}) and determined to be 2.89 eV for TST, 2.66 eV for PHI, and 2.68 eV for AuNSs–PHI, respectively. These E_{BG} values aligned well with their respective band edge wavelengths signifying the viability of PHI and AuNSs–PHI as photocatalysts absorbing visible light. Given that the photochemical effectiveness of a photocatalyst relies on the positions of the conduction band (CB) and valence band (VB), the calculations for TST, PHI, and AuNSs–PHI were conducted using the methodology outlined by Liu *et al.*[52] The estimated valence band energies (E_{VB}) for TCT, PHI, and AuNSs–PHI measured using UPS spectra (Fig. S26, ESI†), are −6.12, −6.6, and −7.00 eV to E_{vacuum}, respectively. Utilizing the calculated E_{BG} values, the conduction band edge/energy (E_{CB}) of TST, PHI, and AuNSs–PHI has been determined as −3.23 eV, −3.94 eV, and −4.36 eV, respectively, as illustrated in Fig. 4e. This established band structure indicates a positive shift in the band positions for AuNSs–PHI compared to TST, aligning energy levels more favourably for solar-assisted O₂ reduction to produce H₂O₂ and the oxidation of organic molecules. The more positive conduction band value in AuNSs–PHI potentially

enhances its capability for selective oxygen reduction reactions, leading to the production of substantial amounts of H₂O₂, as discussed later in this manuscript.

Additionally, the TGA-DSC thermograms are presented in Fig. 4f and Fig. S1c, d, S27, ESI† offer insights into the thermal stability, decomposition characteristics, and atmospheric gas adsorption ability/hydrophilicity of these materials. Notably, the plasmonic photocatalyst AuNSs–PHI demonstrated substantial gas adsorption, exhibiting over 6% weight loss below 50 °C and nearly 16% on reaching 150 °C (Fig. 4f, inset thermogram). This material remains stable up to 650 °C. Moreover, N₂ adsorption–desorption isotherms (Fig. S28 and S29, ESI†) recorded at 77 K provide crucial information about the surface area, pore size distribution, and porosity of the materials. Loading Au nanostars on the PHI surface (AuNSs–PHI) results in an increase in surface area (Table S2, ESI†). The increase in surface area upon loading Au nanostars onto the PHI surface may contribute to improved photocatalytic performance by providing more active sites for reactions.

Ex situ X-ray photoelectron spectroscopy (XPS) was employed for surface chemical composition analysis of the molecular photocatalysts TST and PHI, as well as to determine the oxidation states of surface-loaded plasmonic gold nanostars. The XPS survey spectra confirm the presence of C, N, O, K, Cl,

and Li elements in the PHI framework (Fig. S30, ESI†) and the successful loading of Au nanostars over it (Fig. 5), whereas only C, N, and O were detected in TST (Fig. S31, ESI†). Furthermore, a noticeable rise in oxygen concentration in PHI and AuNSs–PHI, as compared to TST (Fig. S32, ESI†), is consistent with TGA analysis results (Fig. 4f) suggesting significant adsorption of atmospheric oxygen on the surfaces of PHI and AuNSs–PHI, thereby contributing to a heightened rate of SORR. The high-resolution C 1s spectra of AuNSs–PHI (Fig. 5 C 1s) and PHI (Fig. S30 C 1s, ESI†) exhibited six deconvoluted peaks, in

contrast to TST (Fig. S31 C 1s, ESI†) which displayed only three peaks. The binding energy peaks centred around 288.4 and 284.8 eV are attributed to C atoms in aromatic N–C≡N structures and graphitic C–C, respectively, present in all three samples.[40] An additional binding energy peak centred at 286.5 eV associated with –C≡N is observed in the C 1s spectrum of AuNSs–PHI and PHI, confirming the –C≡N functionalization as supported by FTIR analysis (Fig. 3b).[53] The peaks at 285.9 eV and 284.8 eV correspond to the C–O and adventitious C–C bonds, respectively. The high-resolution
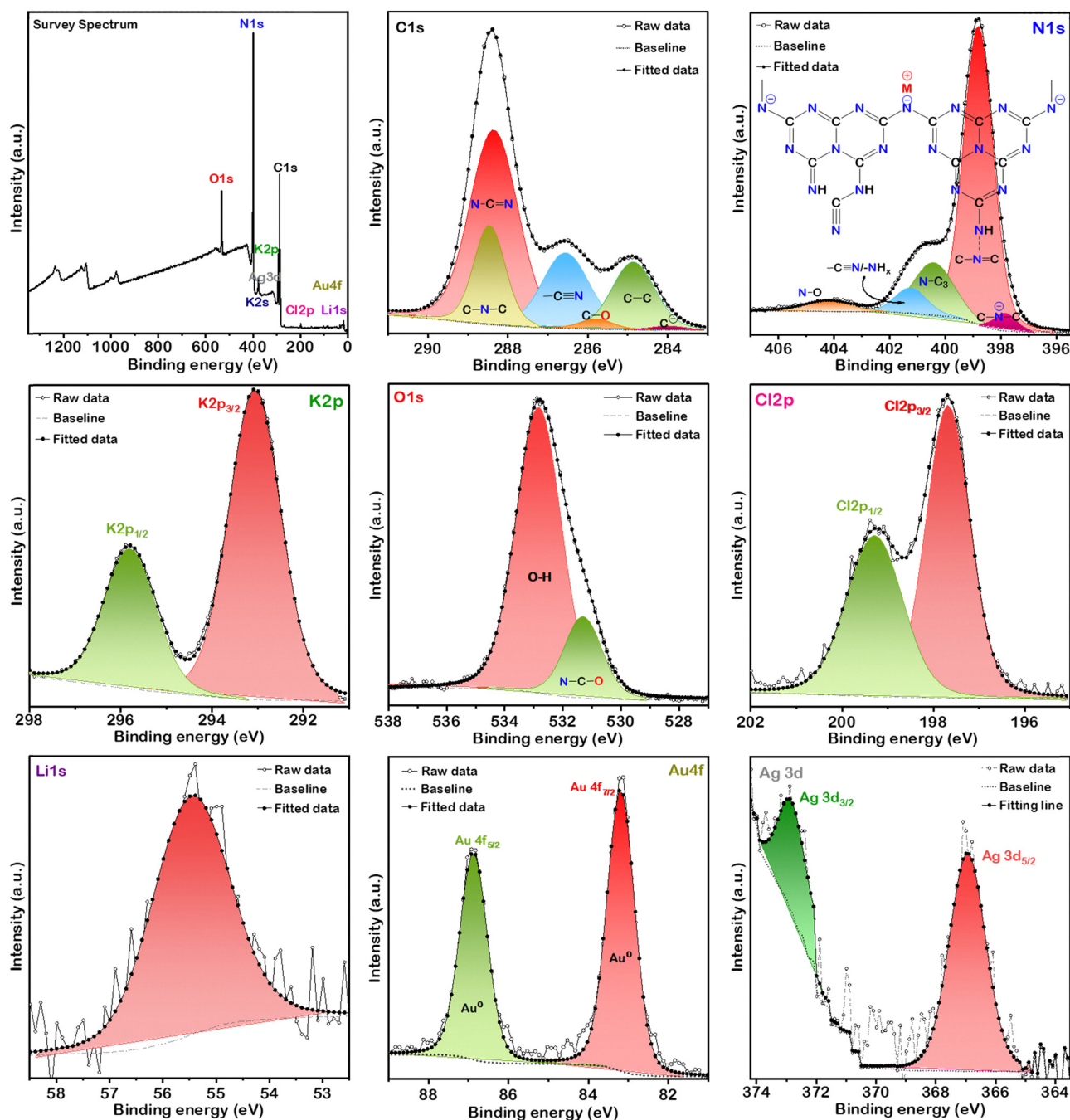

Fig. 5 Electronic state identification of AuNSs–PHI. Survey and core-level XPS spectra for C 1s, N 1s, K 2p, O 1s, Cl 2p, Li 1s, Au 4f and Ag 3d present in AuNSs–PHI.

N 1s XPS spectrum for AuNSs–PHI (Fig. 5 N 1s) reveals five peaks: the peaks at 398.7 and 400.3 eV are attributed to N atoms within C–N=C and N–(C)$_3$ in heptazine units, while the peak at 401.2 eV assigned to N atoms in –C≡N species. The varied binding energies for different nitrogen species in AuNSs–PHI are a result of structural changes induced by –C≡N, negatively charged N, alkali metal incorporation, and the presence of plasmonic Au nanostars.[53] As corroborated by the FT-IR spectra for AuNSs–PHI in Fig. 3b and Fig. S18, ESI,† the presence of bridging negatively charged nitrogen to the heptazine units (C2–N$^{\ominus}$M$^{\oplus}$) is confirmed by XPS, with a peak at 397.8 eV, as shown and labelled in the poly(heptazine imide) structure in Fig. 5 N 1s. The labelled high-resolution N 1s spectra for PHI and TST, presented in Fig. S30 and S31, ESI,† respectively, distinctly illustrate the variation in their chemical structure compared to AuNSs–PHI (Fig. 5 N 1s). XPS results confirm the heptazine frameworks in PHI, with evidence of K presence indicated by doublet peaks at 293.0 and 295.8 eV in the K 2p spectra (Fig. 5 K 2p), displaying a doublet separation of 2.8 eV. The XPS spectra of Cl 2p and Li 1s further affirm the existence of Cl and Li in the PHI framework (Fig. 5). The Au 4f spectrum (Fig. 5 Au 4f) unequivocally confirms the metallic state of the Au nanostars loaded on the PHI surface in the AuNSs–PHI sample. The high-resolution Ag 3d spectrum of AuNSs–PHI (Fig. 5 Ag 3d) reveals the presence of a trace amount of silver, originating from the use of silver ions that serve as nucleation sites, initiating the formation of gold nanoparticles and providing a preferential starting point for subsequent Au ion reduction and AuNSs growth. The electronic and coordination structures of Au species in the AuNSs–PHI plasmonic photocatalyst were further validated through X-ray absorption near-edge structure (XANES) and extended X-ray absorption fine structure (EXAFS) analysis, with comparisons made to Au$_2$O$_3$ and Au foil as references. Au L$_3$ XANES was employed to distinguish between oxidized and reduced forms of the metal. The normalized XANES spectra presented in Fig. 6a reveal that the white line edge intensity of Au species in AuNSs–PHI is significantly lower than that of Au$_2$O$_3$ (Au^{3+}) and nearly identical to the Au foil (Au^0) reference. This confirms the existence of Au nanostars in a metallic state, consistent with the XPS results (Fig. 5 Au 4f). Although the spectrum for Au nanostars loaded on PHI closely resembles that of Au foil in terms of shape and energies, there are slight intensity reductions and positive energy shifts (Fig. 6a inset spectra), possibly indicating a reduction in the Au–Au coordination number for the Au nanostars. This reduction in coordination number leads to a decrease in Au–Au bond distances and a shift in spectral features to higher energies. The Fourier transforms of k^3-weighted EXAFS oscillations of Au foil and AuNSs–PHI, measured at the Au L$_3$ edge are depicted in Fig. 6b. The peaks at 2.49 and 2.79 Å for both Au foil and AuNSs–PHI indicate that the Au nanostars remained in a metallic state on AuNSs–PHI.[54,55] The corresponding EXAFS $\chi(k)$ signals in k-space spectra (Fig. 6c) show that the phase in the oscillation of Au from AuNSs–PHI does not exhibit any shift from Au foil, indicating that the atomic structure remains identical to Au bulk, strengthening this conclusion.

The presence of metallic AuNSs is further confirmed through Fourier transform analysis of extended X-ray absorption fine structure (FT-EXAFS) spectra in the R-space of Au, alongside reference materials (Fig. 6d). Notably, the FT-EXAFS analysis of AuNSs–PHI indicates that the loading of Au stars onto PHI does not alter its metallic state. Wavelet transform contour spectra in Fig. 6e provide additional confirmation of the absence of Au–O bonds and pure metallic character of Au nanostars loaded over PHI. A distinct feature centred at k space of $\sim$12.6 Å^{-1}, indicative of Au–Au bonds, is observed when compared to Au$_2$O$_3$, Au foil, and AuNSs–PHI. This observation aligns with the results of XPS analyses, reinforcing the conclusion that AuNSs–PHI contains only metallic Au.

Scanning electron microscopy (SEM) and transmission electron microscopy (TEM) images depict the morphologies of pristine TST (Fig. S33, ESI†), PHI (Fig. S9 PHI, ESI† and Fig. 7a), and AuNSs–PHI (Fig. S10–S16, ESI† and Fig. 7d–g), showcasing thin sheet-like structures, nanoflakes, and Au nanostars loaded nanoflakes. The SEM images (Fig. 7a and Fig. S3, ESI†) of PHI reveal a distinctive morphology characterized by vertically aligned nanoflakes resembling grass blades. This structural arrangement is further illustrated in the accompanying schematic (Fig. S34, ESI†). In addition, detailed electron microscopy images (Fig. 7, and multiple Supplementary Figures, ESI†) depict Au$_{seed}$, Au nanostars of diverse sizes, and AuNSs–PHI with varying amounts of Au nanostar loading, emphasizing a remarkable precision in their size control and a consistent distribution across the PHI surface. This uniformity underscores the effectiveness of the synthesis process in achieving precise and well-distributed structures. The bulk EDS spectra of PHI and AuNSs–PHI, as depicted in Fig. 7h, are complemented by corresponding EDS maps (Fig. 7i) showcasing the elemental distribution of Au, C, K, and N. This combined spectroscopic and visual mapping analysis firmly confirms the successful loading of Au nanostars and the integration of alkali metals into the PHI framework. The HRTEM image of individual PHI particles (Fig. 7j), along with the corresponding Fast Fourier transform (FFT) pattern in the inset, stands as compelling evidence affirming the crystalline nature of PHI. Notably, characteristic distances of 10.4 Å, corresponding to the (−110) plane in poly(heptazine imide), and 6.06 Å, corresponding to the (−210) plane, were identified. The HRTEM micrograph (Fig. 7j) displays a selected fringe for d-spacing calculations of PHI, which is accentuated in the profile plot. Fig. 7k shows a plot of the intensity values of a line perpendicular to these fringes, accentuating the precision of the performed d-spacing measurements.

As evident from XPS (Fig. 5 Au 4f) and X-ray Absorption Spectroscopy (XAS) (Fig. 6), the synthesized Au nanostars exhibit a notable absence of any other chemical or oxidized impurities. This assertion is further substantiated by the HR-TEM micrographs and FFT pattern presented in Fig. 7l, where lattice fringes attest to the high crystallinity of these plasmonic Au nanostars loaded on PHI, enabling precise determination of the inter-planar spacing. The calculated d-spacing of 2.33 Å, corresponding to the {111} lattice plane of gold, as depicted in
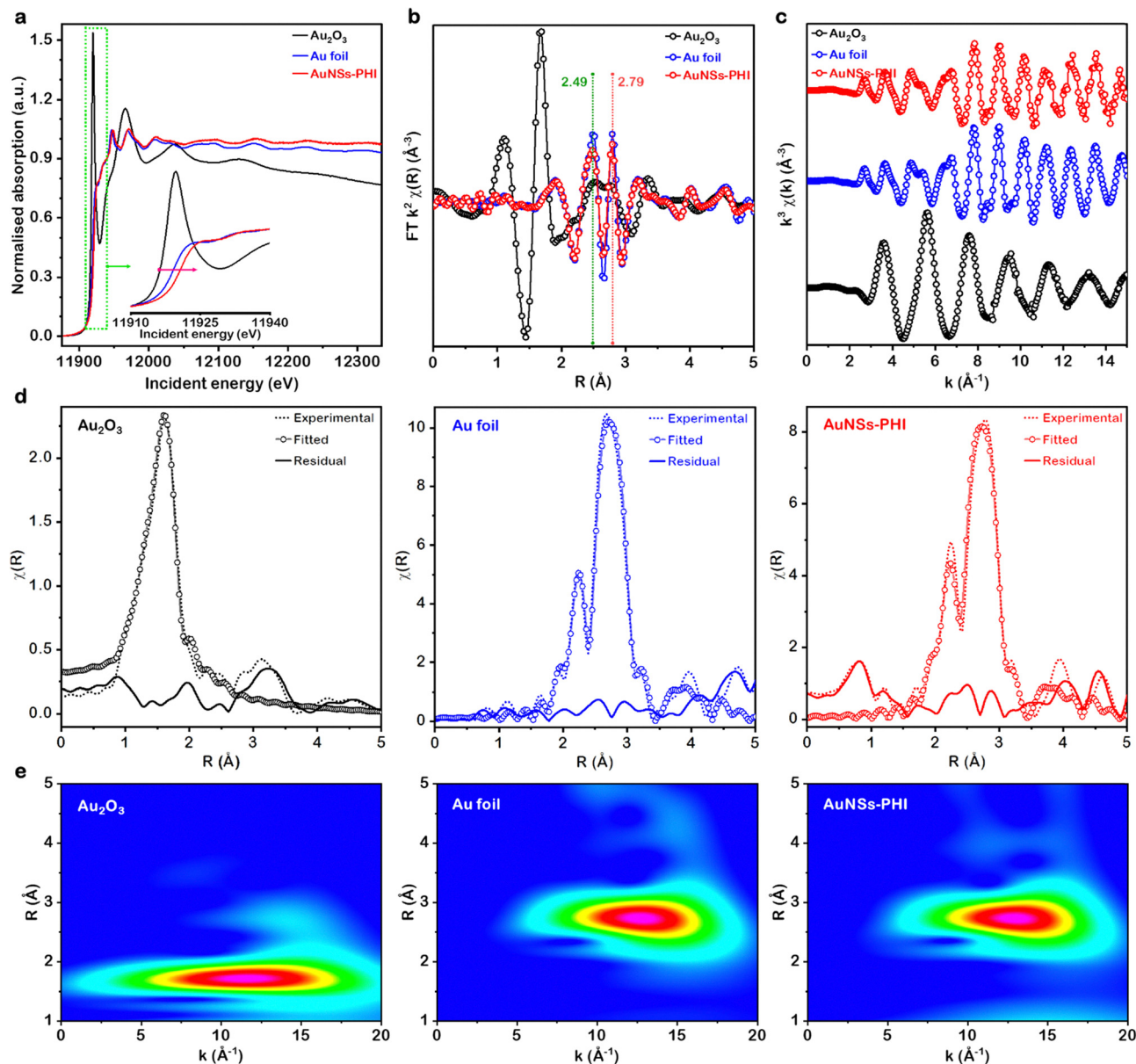
Fig. 6 X-ray absorption fine structure (XAFS) measurement at the Au L$_3$ edge. (a) Normalised XANES spectra of AuNSs−PHI, and reference samples (Au$_2$O$_3$ and Au foil) at the Au L$_3$ edge. (b) Fourier transformed (FT) k^3-weighted $\chi(k)$ function of the EXAFS spectra of AuNSs−PHI, Au$_2$O$_3$ and Au foil. (c) EXAFS $\chi(k)$ signals in k-space. (d) FT-EXAFS of Au$_2$O$_3$, Au foil, and AuNSs−PHI with experimental and fitted spectra. (e) Wavelet transform k^3-weighted EXAFS spectra of Au$_2$O$_3$, Au foil, and AuNSs−PHI.

the d-spacing calculation plot profile (Fig. 7m), aligns closely with the results reported in the XRD pattern (Fig. 3a).

Solar-driven O$_2$ reduction to H$_2$O$_2$

First, a thorough investigation was conducted on the performance of PHI under solar simulator light conditions (AM 1.5) using the DPD colorimetric method (ESI†). Fig. 8a (line graph with solid circle symbols) shows the cumulative solar H$_2$O$_2$ production profiles over time, revealing a significant rise in the accumulated H$_2$O$_2$ concentration as the amount of PHI in suspension increased. Specifically, the concentration elevated from 40.3 mM H$_2$O$_2$ for a 0.125 g L^{-1} PHI suspension to 98.0 mM H$_2$O$_2$ for a 2.0 g L^{-1} PHI suspension after 2 h of

irradiation. Surprisingly, the H$_2$O$_2$ production rate (mM g^{-1} h^{-1}) exhibited a contrarian trend, showcasing a decline with increasing PHI concentration (Fig. 8a column graph). Despite the lower accumulated H$_2$O$_2$ concentrations, the optimal suspension concentration for the highest production rate was identified as 0.125 g L^{-1}, generating H$_2$O$_2$ at a rate of 161.3 mM g^{-1} h^{-1}. This result highlights the intricate interplay between catalyst concentration and production rate, offering insights for optimising the solar-driven H$_2$O$_2$ production process with PHI as the photocatalyst. The decrease in H$_2$O$_2$ production rate at high photocatalyst concentrations is likely caused by factors such as PHI agglomeration, diminishing the effective surface area for photochemical reactions, and increased light scattering, which reduces solar
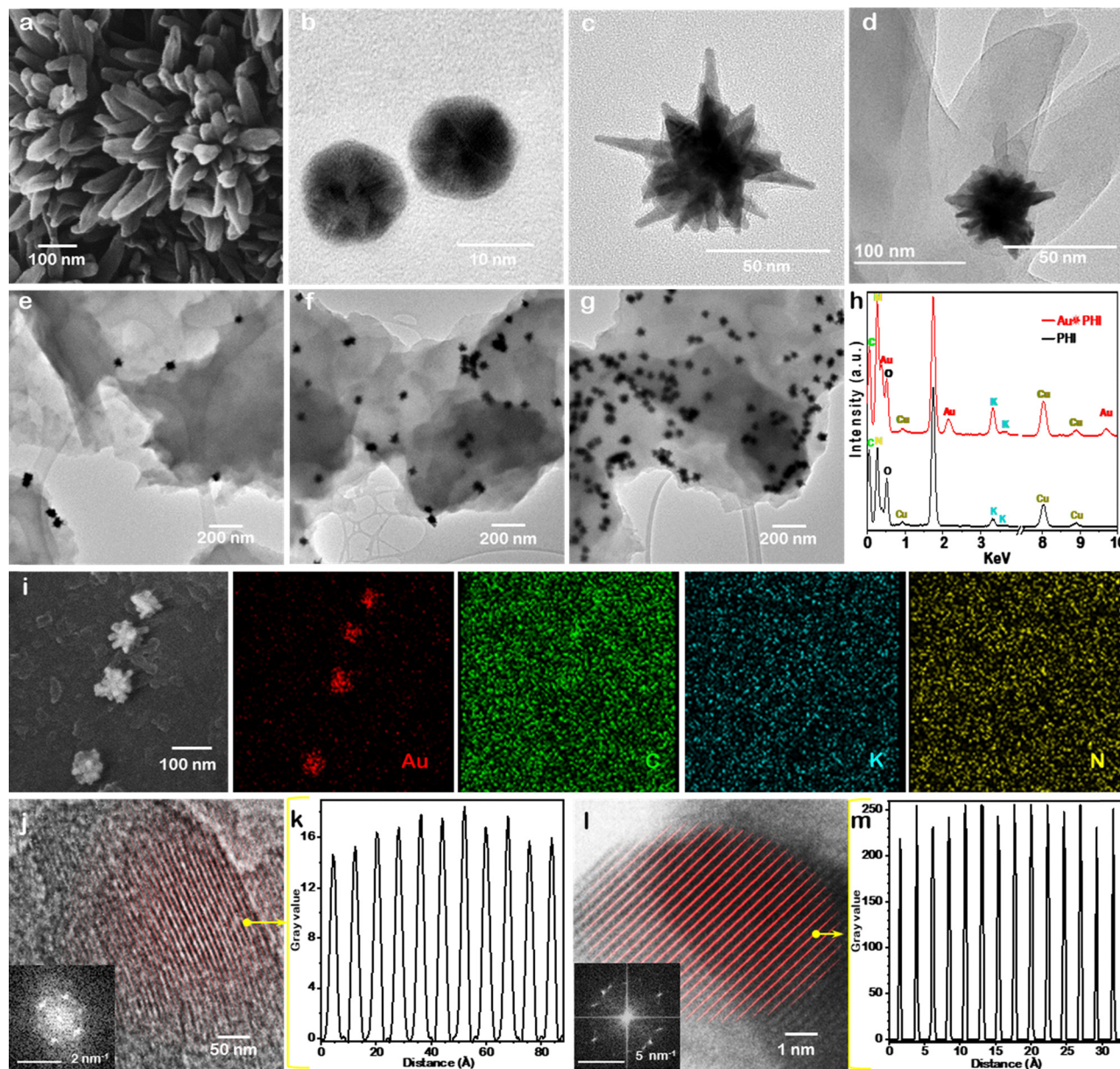
Fig. 7 Electron microscopy (EM) studies. EM image of PHI (a), Au seed (b), individual Au star (size ~ 80 nm) (c), and Au star grown on PHI (AuNSs–PHI) (d). TEM images showcase the distribution of Au stars on PHI, derived from three varying concentrations of gold precursor: (e) 0.15 wt% AuNSs–PHI, (f) 0.30 wt% AuNSs–PHI, and (g) 0.60 wt% AuNSs–PHI. (h) A comparison is made between the bulk EDS spectra of pristine PHI and Au star-decorated PHI (AuNSs–PHI). (i) SEM image and corresponding EDS maps for gold, carbon, potassium, and nitrogen for AuNSs–PHI. HRTEM image of individual PHI particles (j) accompanied by the corresponding fast Fourier transform (FFT) pattern (in the inset image), along with a profile plot for determining d-spacing (k). Similarly, an HRTEM image of a single Au star (l) is provided, along with its corresponding FFT (in the inset image), and a profile plot for calculating d-spacing (m).

radiation penetration. Furthermore, higher concentrations may impede the effective transport of O_2/organic molecules to the photocatalytic sites, potentially leading to self-degradation of the photogenerated H_2O_2.

The structurally modulated, light-absorption-enhanced, surface-functionalized, and alkali metal-incorporated poly(heptazine imide) structured g-C_3N_4 (PHI) demonstrated a very high H_2O_2 production rate of 161.3 mM g^{-1} h^{-1} (Fig. 8a). Moreover, integrating plasmonic Au nanostars in the construction of plasmonic-photocatalysts is advantageous, as the inclusion of

gold as a co-catalyst has proven to be an excellent catalyst for solar H_2O_2 production without promoting the decomposition of photogenerated H_2O_2.[56–58] Consequently, 0.3 wt% Au incorporation in plasmonic AuNSs–PHI photocatalyst resulted in up to two-fold increase in the H_2O_2 production rate (286.95 mM g^{-1} h^{-1}) compared to PHI (161.3 mM g^{-1} h^{-1}) and an eleven-fold increase compared to TST (25.76 mM g^{-1} h^{-1}) under UV-visible irradiation (Fig. 8b). As previously discussed (Fig. S20, ESI†), this substantial enhancement in photocatalytic performance for AuNSs–PHI is primarily attributed to the localized surface plasmon resonance
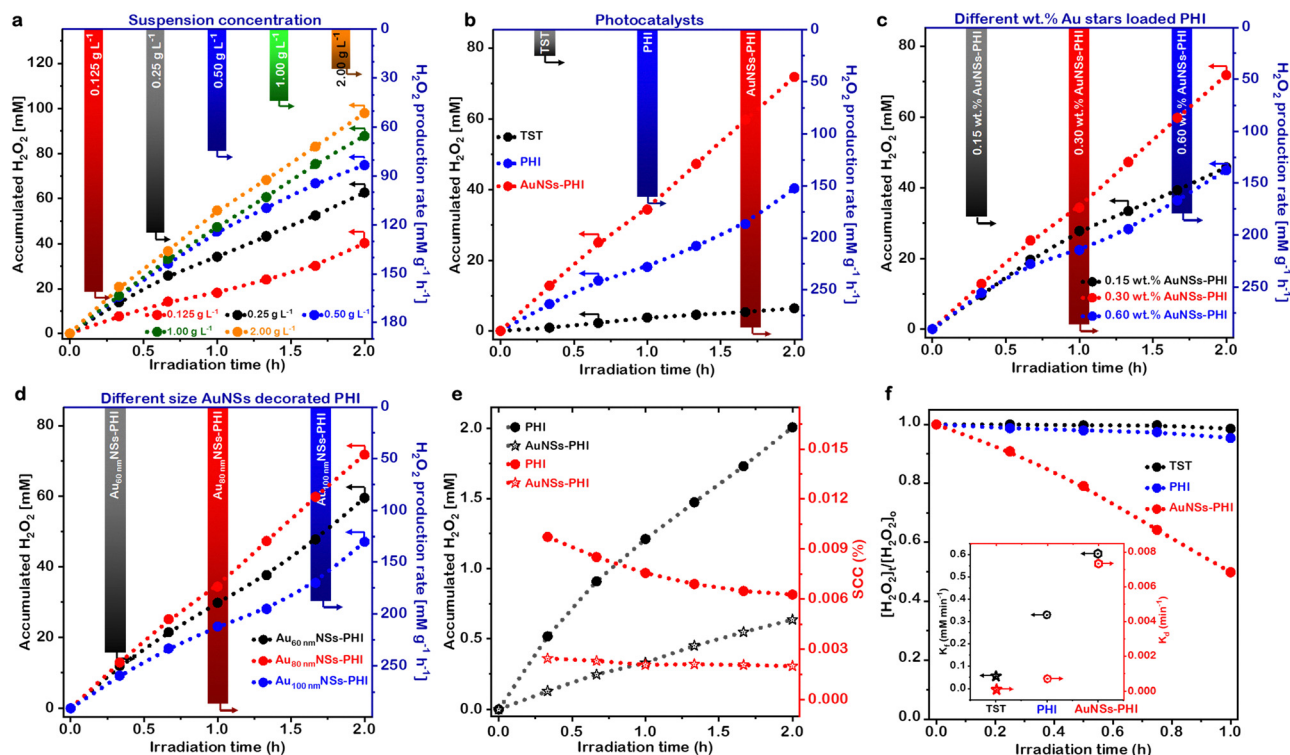
Fig. 8 Highly efficient and stable SORR over the plasmonic photocatalysts. (a) Cumulative production of H_2O_2 over time (presented as a line graph with symbols) and the production rate (illustrated as a column graph) are shown for various suspension concentrations of PHI in a 50 vol% i-PrOH. (b) Typical time course H_2O_2 production, and production rate over TST, pristine PHI, and AuNSs–PHI (around 80 nm 0.30 wt% Au nanostars loaded PHI). (c) Cumulative production of H_2O_2 over time (line graph with symbols) and the production rate (column graph) are shown for various wt% Au nanostars (size around 80 nm) loaded PHI (AuNSs–PHI) in a 50 vol% i-PrOH. (d) Investigating how the size of Au nanostars, with a loaded concentration of 0.30 wt%, influences H_2O_2 production in a 50 vol% i-PrOH for PHI. (e) Time profiles of solar-driven H_2O_2 production and solar-to-chemical conversion (SCC) efficiency from H_2O and O_2 examined for both PHI and AuNSs–PHI. (f) Photochemical H_2O_2 decomposition under UV-visible light irradiation. Photochemical H_2O_2 formation (k_F) and decomposition (k_D) kinetics constant (inset graph).

effect of Au nanostars, coupled with the synergistic impact of their star morphology, strong electromagnetic field properties, and optical characteristics. Additionally, to identify the optimal plasmonic Au nanostars concentration loading onto PHI, two new AuNSs–PHI samples with a higher (*i.e.* 0.60 wt% Au nanostars) and a lower (*i.e.* 0.15 wt% Au nanostars) Au loading were synthesized and studied for SORR. The results are reported in Fig. 8c. The decrease in the H_2O_2 production rate at higher Au nanostars loading beyond 0.3% wt is probably due to the saturation of plasmon absorption, resulting in diminishing returns. Moreover, the elevated Au nanostars loading is seen to cover a large amount of photocatalyst surface, potentially hindering light penetration and limiting the accessibility of reactants to the active sites on the PHI surface. Similarly, the effect of Au nanostar size (with fixed wt% of Au, *i.e.*, 0.30 wt% Au) on H_2O_2 production rate was also investigated, shown in Fig. 8d. From this figure, we observe a that the H_2O_2 production rate increases for ~80 nm Au nanostar-loaded PHI (Au_{80nm}NSs–PHI or AuNSs–PHI in Fig. 8c) compared to ~60 nm Au nanostar-loaded PHI (Au_{60nm}NSs–PHI). Larger Au nanostars (~100 nm, Au_{100nm}NSs–PHI) result however in a decline in H_2O_2 production rate compared to AUNSs <100 nm.

The performance of AuNSs–PHI and PHI for solar radiation-driven H_2O_2 generation from O_2 and water, without the use of

any sacrificial agent, was evaluated to underscore the potential of plasmonic photocatalysts for unassisted solar fuel production (Fig. 8e). AuNSs–PHI exhibited a noteworthy solar H_2O_2 production of 0.63 mM after 2 hours of light irradiation.[56,59] The relatively low solar H_2O_2 production and solar-to-chemical conversion (SCC) efficiency in the absence of a sacrificial agent could be attributed to the consecutive decomposition of photogenerated H_2O_2 on the AuNSs–PHI surfaces during the photochemical reaction. Nevertheless, ongoing efforts involve developing a strategy to partially cover AuNSs–PHI with a conductive hydrophobic material to minimize surface adsorption of photogenerated H_2O_2, thereby restricting its participation in any subsequent oxidation reaction following its production.[10]

The kinetics of the two-electron, solar-driven oxygen reduction reaction ($2e^-$ SORR) to H_2O_2 over plasmonic photocatalyst AuNSs–PHI, as well as two other photocatalysts (PHI and TST), were explored using the kinetic model for photochemical H_2O_2 generation during the initial phase of the reaction, as reported by Hoffmann *et al.*: $[H_2O_2] = (k_F/k_D)(1 - e^{-k_D t}) + [H_2O_2]_0 e^{-k_D t}$.[60,61] In this model, k_F and k_D represent the rate constants for the photochemical H_2O_2 formation and decomposition reactions, respectively. The reaction kinetics revealed a

zero-order rate for H_2O_2 formation under continuous O_2 purging, while the photodecomposition reaction exhibited first-order kinetics with a fixed initial H_2O_2 concentration. The k_D value for AuNSs–PHI (0.00734 min^{-1}) (Fig. 8f inset) was higher than that of the base photocatalyst PHI (0.000705 min^{-1}) and the reference photocatalyst TST (0.0000943 min^{-1}), indicating a significantly faster H_2O_2 decomposition rate for AuNSs–PHI sample. Additionally, a higher k_F value of 0.60473 mM min^{-1} on AuNSs–PHI suggested that solar H_2O_2 production is primarily governed by the formation kinetics, highlighting the substantial contribution of plasmonic Au nanostars in this process. The AuNSs–PHI plasmonic photocatalyst demonstrated a significantly higher (7 folds higher than K-PHI) solar H_2O_2 production rate compared to a wide range of photocatalysts (Fig. S38, ESI†), including metal oxides,[62–64] metal sulfides,[65,66] carbon nitrides,[67–69] metal organics[70–72] and COF.[73,74]

To unravel the kinetics and electron transfer number (n) involved in the oxygen reduction reaction for H_2O_2 production, we conducted decisive linear sweep voltammetry (LSV) experiments in 0.1 M KOH electrolyte under continuous O_2 purging (Fig. S39a–c, ESI†). Analysing the current curves using the Koutecky–Levich (K–L) equation and examining the linearly fitted K–L plots for AuNSs–PHI, PHI, and TST in Fig. S39d–f, ESI,† respectively, provided crucial insights. The slope of these K–L plots decisively revealed the overall electron transfer number for the oxygen reduction reaction (ORR). The calculated electron participation in ORR at different potentials in Fig. S40, ESI† affirmatively demonstrates an average value of n as 2.08 for AuNSs–PHI, unequivocally confirming the selective two-electron ORR pathway leading to H_2O_2 production over its surface. The two photocatalysts, PHI and TST, similarly exhibit 2e$^-$ ORR kinetics, with relatively lower electron transfer numbers (1.80 for PHI and 1.52 for TST) (Fig. S40, ESI†). This finding aligns with the established trend of the selective two-electron pathway for ORR in these materials, providing valuable insights into their electrocatalytic behaviour for H_2O_2 production.

Although isopropanol was used here to facilitate the photoreduction of O_2, recent findings have highlighted that the choice of sacrificial agents and solvents can significantly alter reaction pathways and product selectivity.[75] In particular, organic proton donors such as alcohols may induce side reactions and mask intrinsic photocatalytic behaviour, thus overestimating the apparent H_2O_2 yield.[75] These insights suggest the need for evaluating photocatalytic performance in more realistic, sacrificial-agent-free systems. Additionally, challenges associated with H_2O_2 separation and accumulation remain significant obstacles for real-world deployment, where gas–solid photocatalytic systems could offer potential solutions.[76]

optimized 0.3 wt% $\sim$80 nm Au nanostars-decorated PHI (AuNSs–PHI) exhibited a high solar-driven H_2O_2 production rate of 286.95 mM g^{-1} h^{-1}. Experimental and theoretical analyses confirmed the metallic character of Au nanostars and the surface functionality of PHI, demonstrating their potential for sustainable H_2O_2 production via surface-oriented reduction reactions. We also carried out TD-DFT calculations in which a small Au cluster was modelled on a PHI slab using the PBE functional, and the projected density of states (PDOS) was analysed. The results show that the Fermi level of the Au cluster lies above the conduction band edge of PHI, indicating that, upon plasmon excitation, PHI has energetically accessible states to receive hot electrons. This alignment energetically favors the transfer of hot electrons from Au into PHI. Additionally, the calculations reveal the formation of hybridized states at the Au–PHI interface, which could further facilitate interfacial charge transfer. However, we acknowledge the inherent limitations of our DFT approach in fully capturing the complexity of LSPR-induced hot electron dynamics in anisotropic Au nanostructures (AuNSs). Additionally, this work highlights an innovative and sustainable approach to reuse isopropanol (isopropyl alcohol or i-PrOH) waste for H_2O_2 production, leveraging natural resources while minimizing environmental impact. This approach aligns with circular economy principles, reducing the carbon footprint associated with isopropanol waste. Overall, our findings represent a significant advancement in plasmonic-photocatalyst heterostructures, offering promising applications in energy conversion, environmental remediation, and in situ heterogeneous catalysis. This work paves the way for the scalable and sustainable production of H_2O_2 through plasmon-enhanced photocatalysis.

Author contributions

P. S. conceptualized and synthesized 3D PHI nanostructures, carried out advanced characterisation of the AuNSs–PHI materials, investigated H_2O_2 production performance and wrote the first draft of the manuscript. K. E. synthesized plasmonic Au nanoparticles, Au nanostars and AuNSs–PHI photocatalysts, carried out electron microscopy studies, and finalised the manuscript. M. D. modelled the structure of PHI, did band structure analysis, and further theoretical studies of plasmonic enhancement. R. A. C. supervised computational studies. T. H. provided theoretical insights and support, and critically reviewed and revised the manuscript. A. B. and A. Z. performed transient measurements to gain insight into the generation of hot carriers. M. W. performed XAS analysis. F. X. conceptualised and supervised the project. All authors reviewed and commented on the manuscript.

Summary and conclusions

In this study, we developed a highly photoactive photocatalyst by integrating plasmonic Au nanostars with PHI nanoflakes, achieving outstanding photocatalytic H_2O_2 production. The

Conflicts of interest

There are no conflicts to declare.

Data availability

The data supporting the findings of this study are provided in the ESI.† Additional datasets generated are available from the corresponding authors upon reasonable request.

References

1 R. L. Myers, *The 100 most important chemical compounds: a reference guide*, 2007.

2 Y.-J. Lin, I. Khan, S. Saha, C.-C. Wu, S. R. Barman, F.-C. Kao and Z.-H. Lin, *Nat. Commun.*, 2021, **12**, 180.

3 S. J. Freakley, S. Kochius, J. van Marwijk, C. Fenner, R. J. Lewis, K. Baldenius, S. S. Marais, D. J. Opperman, S. T. L. Harrison, M. Alcalde, M. S. Smit and G. J. Hutchings, *Nat. Commun.*, 2019, **10**, 4178.

4 R. J. Lewis, K. Ueura, X. Liu, Y. Fukuta, T. E. Davies, D. J. Morgan, L. Chen, J. Qi, J. Singleton, J. K. Edwards, S. J. Freakley, C. J. Kiely, Y. Yamamoto and G. J. Hutchings, *Science*, 2022, **376**, 615–620.

5 M. Ko, Y. Kim, J. Woo, B. Lee, R. Mehrotra, P. Sharma, J. Kim, S. W. Hwang, H. Y. Jeong, H. Lim, S. H. Joo, J. W. Jang and J. H. Kwak, *Nat. Catal.*, 2022, **5**, 37–44.

6 C. Xia, Y. Xia, P. Zhu, L. Fan and H. Wang, *Science*, 2019, **366**, 226–231.

7 D. W. Flaherty, *ACS Catal.*, 2018, **8**, 1520–1527.

8 J. H. Kim, D. Hansora, P. Sharma, J.-W. Jang and J. S. Lee, *Chem. Soc. Rev.*, 2019, **48**, 1908–1971.

9 H. Song, S. Luo, H. Huang, B. Deng and J. Ye, *ACS Energy Lett.*, 2022, **7**, 1043–1065.

10 Y. Hong, Y. Cho, E. M. Go, P. Sharma, H. Cho, B. Lee, S. M. Lee, S. O. Park, M. Ko, S. K. Kwak, C. Yang and J.-W. Jang, *Chem. Eng. J.*, 2021, **418**, 129346.

11 T. Liu, Z. Pan, J. J. M. Vequizo, K. Kato, B. Wu, A. Yamakata, K. Katayama, B. Chen, C. Chu and K. Domen, *Nat. Commun.*, 2022, **13**, 1034.

12 P. Sharma, T. J. A. Slater, M. Sharma, M. Bowker and C. R. A. Catlow, *Chem. Mater.*, 2022, **34**, 5511–5521.

13 C. Ji, J. Xu, Q. Jiang, G. Kerherve, H. Zhou, X. Li, S. Tang, P. Sharma, D. J. Riley and F. Xie, *Mater. Today Adv.*, 2023, **18**, 100361.

14 H. Hou, X. Zeng and X. Zhang, *Angew. Chem., Int. Ed.*, 2020, **59**, 17356–17376.

15 Y. Sun, L. Han and P. Strasser, *Chem. Soc. Rev.*, 2020, **49**, 6605–6631.

16 C.-H. Bao, L. Li, X.-F. Wang, S.-S. Xia, X. Wang, C.-C. Jin and Z. Chen, *Nano Lett.*, 2025, **25**(11), 4115–4136.

17 H. L. Tan, C. H. T. Chai, J. Z. X. Heng, Q. V. Thi, X. Wu, Y. H. Ng and E. Ye, *Adv. Sci.*, 2025, **12**, 2407801.

18 Y. Tang, W. Wang, J. Ran, C. Peng, Z. Xu and W. Chu, *Energy Environ. Sci.*, 2024, **17**, 6482–6498.

19 W. Xue, J. Ye, Z. Zhu, R. Kumar and J. Zhao, *Energy Environ. Sci.*, 2025, **18**, 214–226.

20 H. Ling, H. Sun, L. Lu, J. Zhang, L. Liao, J. Wang, X. Zhang, Y. Lan, R. Li, W. Lu, L. Cai, X. Bai and W. Wang, *Nat. Commun.*, 2024, **15**, 9505.

21 L. Yuan, M. Lou, B. D. Clark, M. Lou, L. Zhou, S. Tian, C. R. Jacobson, P. Nordlander and N. J. Halas, *ACS Nano*, 2020, **14**, 12054–12063.

22 C. R. Jacobson, G. Wu, L. B. Alemany, G. N. Naidu, M. Lou, Y. Yuan, A. Bayles, B. D. Clark, Y. Cheng, A. Ali, A.-L. Tsai, I. A. Tonks, P. Nordlander and N. J. Halas, *Nano Lett.*, 2022, **22**, 5570–5574.

23 Y. Xin, K. Yu, L. Zhang, Y. Yang, H. Yuan, H. Li, L. Wang and J. Zeng, *Adv. Mater.*, 2021, **33**, 1–26.

24 A. Campos, N. Troc, E. Cottancin, M. Pellarin, H. C. Weissker, J. Lermé, M. Kociak and M. Hillenkamp, *Nat. Phys.*, 2019, **15**, 275–280.

25 H. E. Lee, H. Y. Ahn, J. Mun, Y. Y. Lee, M. Kim, N. H. Cho, K. Chang, W. S. Kim, J. Rho and K. T. Nam, *Nature*, 2018, **556**, 360–364.

26 P. Wang, A. V. Krasavin, L. Liu, Y. Jiang, Z. Li, X. Guo, L. Tong and A. V. Zayats, *Chem. Rev.*, 2022, **122**, 15031–15081.

27 M. Sayed, J. Yu, G. Liu and M. Jaroniec, *Chem. Rev.*, 2022, **122**, 10484–10537.

28 H. A. Atwater and A. Polman, *Nat. Mater.*, 2010, **9**, 205–213.

29 A. N. Koya, X. Zhu, N. Ohannesian, A. A. Yanik, A. Alabastri, R. Proietti Zaccaria, R. Krahne, W.-C. Shih and D. Garoli, *ACS Nano*, 2021, **15**, 6038–6060.

30 Y. Zhang, Q. Pan, G. Chai, M. Liang, G. Dong, Q. Zhang and J. Qiu, *Sci. Rep.*, 2013, **3**, 1943.

31 N. Liu, T. Li, Z. Zhao, J. Liu, X. Luo, X. Yuan, K. Luo, J. He, D. Yu and Y. Zhao, *ACS Omega*, 2020, **5**, 12557–12567.

32 H. Schlomberg, J. Kröger, G. Savasci, M. W. Terban, S. Bette, I. Moudrakovski, V. Duppel, F. Podjaski, R. Siegel, J. Senker, R. E. Dinnebier, C. Ochsenfeld and B. V. Lotsch, *Chem. Mater.*, 2019, **31**, 7478–7486.

33 E. Wirnhier, M. B. Mesch, J. Senker and W. Schnick, *Chem. – Eur. J.*, 2013, **19**, 2041–2049.

34 M. Cui, K. Cui, X. Liu, X. Chen, Y. Chen and Z. Guo, *J. Hazard. Mater.*, 2022, **424**, 127292.

35 Y. Li, H. Xu, S. Ouyang, D. Lu, X. Wang, D. Wang and J. Ye, *J. Mater. Chem. A*, 2016, **4**, 2943–2950.

36 Y. Li, S. Ouyang, H. Xu, X. Wang, Y. Bi, Y. Zhang and J. Ye, *J. Am. Chem. Soc.*, 2016, **138**, 13289–13297.

37 H. Wang, C. Zhao, Z. Burešová, F. Bureš and J. Liu, *J. Mater. Chem. A*, 2023, **11**, 3753–3770.

38 L. Jing, Y. Xu, M. Xie, Z. Li, C. Wu, H. Zhao, N. Zhong, J. Wang, H. Wang, Y. Yan, H. Li and J. Hu, *Small*, 2024, **20**, 1–35.

39 W. Wang, H. Zhang, S. Zhang, Y. Liu, G. Wang, C. Sun and H. Zhao, *Angew. Chem.*, 2019, **131**, 16797–16803.

40 H. Yu, R. Shi, Y. Zhao, T. Bian, Y. Zhao, C. Zhou, G. I. N. Waterhouse, L. Wu, C. Tung and T. Zhang, *Adv. Mater.*, 2017, **29**, 1605148.

41 F. K. Kessler, Y. Zheng, D. Schwarz, C. Merschjann, W. Schnick, X. Wang and M. J. Bojdys, *Nat. Rev. Mater.*, 2017, **2**, 17030.

42 T. Yanai, D. P. Tew and N. C. Handy, *Chem. Phys. Lett.*, 2004, **393**, 51–57.

43 S. Hirata and M. Head-Gordon, *Chem. Phys. Lett.*, 1999, **314**, 291–299.

44 S. M. Dancoff, *Phys. Rev.*, 1950, **78**, 382–385.

45 M. E. Casida, F. Gutierrez, J. Guan, F.-X. Gadea, D. Salahub and J.-P. Daudey, *J. Chem. Phys.*, 2000, **113**, 7062–7071.

46 F. Neese, *Wiley Interdiscip. Rev.: Comput. Mol. Sci.*, 2012, **2**, 73–78.

47 J. Kröger, A. Jiménez-Solano, G. Savasci, P. Rovó, I. Moudrakovski, K. Küster, H. Schlomberg, H. A. Vignolo-González, V. Duppel, L. Grunenberg, C. B. Dayan, M. Sitti, F. Podjaski, C. Ochsenfeld and B. V. Lotsch, *Adv. Energy Mater.*, 2021, **11**, 2003016.

48 W. Xu, X. An, Q. Zhang, Z. Li, Q. Zhang, Z. Yao, X. Wang, S. Wang, J. Zheng, J. Zhang, W. Wu and M. Wu, *ACS Sustainable Chem. Eng.*, 2019, **7**, 12351–12357.

49 Z. Chen, A. Savateev, S. Pronkin, V. Papaefthimiou, C. Wolff, M. G. Willinger, E. Willinger, D. Neher, M. Antonietti and D. Dontsova, *Adv. Mater.*, 2017, **29**, 1700555.

50 Y. Shiraishi, S. Kanazawa, Y. Sugano, D. Tsukamoto, H. Sakamoto, S. Ichikawa and T. Hirai, *ACS Catal.*, 2014, **4**, 774–780.

51 A. Rogolino, I. F. Silva, N. V. Tarakina, M. A. R. da Silva, G. F. S. R. Rocha, M. Antonietti and I. F. Teixeira, *ACS Appl. Mater. Interfaces*, 2022, **14**, 49820–49829.

52 J. Liu, Y. Liu, N. Liu, Y. Han, X. Zhang, H. Huang, Y. Lifshitz, S.-T. Lee, J. Zhong and Z. Kang, *Science*, 2015, **347**, 970–974.

53 W. Wang, H. Zhang, S. Zhang, Y. Liu, G. Wang, C. Sun and H. Zhao, *Angew. Chem., Int. Ed.*, 2019, **58**, 16644–16650.

54 D. M. Chevrier, R. Yang, A. Chatt and P. Zhang, *Nanotechnol. Rev.*, 2015, **4**, 193–206.

55 M. A. MacDonald, D. M. Chevrier, P. Zhang, H. Qian and R. Jin, *J. Phys. Chem. C*, 2011, **115**, 15282–15287.

56 H. Hirakawa, S. Shiota, Y. Shiraishi, H. Sakamoto, S. Ichikawa and T. Hirai, *ACS Catal.*, 2016, **6**, 4976–4982.

57 D. Tsukamoto, A. Shiro, Y. Shiraishi, Y. Sugano, S. Ichikawa, S. Tanaka and T. Hirai, *ACS Catal.*, 2012, **2**, 599–603.

58 R. H. Adnan and A. A. Jalil, *Mater. Today Chem.*, 2023, **27**, 101322.

59 G. Moon, W. Kim, A. D. Bokare, N. Sung and W. Choi, *Energy Environ. Sci.*, 2014, **7**, 4023–4028.

60 C. Kormann, D. W. Bahnemann and M. R. Hoffmann, *Environ. Sci. Technol.*, 1988, **22**, 798–806.

61 A. J. Hoffman, E. R. Carraway and M. R. Hoffmann, *Environ. Sci. Technol.*, 1994, **28**, 776–785.

62 X. Zhang, D. Gao, B. Zhu, B. Cheng, J. Yu and H. Yu, *Nat. Commun.*, 2024, **15**, 3212.

63 Z. Jiang, B. Cheng, Y. Zhang, S. Wageh, A. A. Al-Ghamdi, J. Yu and L. Wang, *J. Mater. Sci. Technol.*, 2022, **124**, 193–201.

64 G. H. Moon, W. Kim, A. D. Bokare, N. E. Sung and W. Choi, *Energy Environ. Sci.*, 2014, **7**, 4023–4028.

65 W. Wang, Z. Chen, C. Li, B. Cheng, K. Yang, S. Zhang, G. Luo, J. Yu and S. Cao, *Adv. Funct. Mater.*, 2025, 2422307.

66 Y.-N. Wang, Y. Guo, J. Peng, J. Zhao, L. Yang, H. Song and C. Chen, *J. Environ. Chem. Eng.*, 2025, **13**, 115296.

67 C. Shi, R. Pan, J. Yuan and C. Liu, *Adv. Funct. Mater.*, 2025, **2500342**, 1–13.

68 C. W. Bai, L. L. Liu, J. J. Chen, F. Chen, Z. Q. Zhang, Y. J. Sun, X. J. Chen, Q. Yang and H. Q. Yu, *Nat. Commun.*, 2024, **15**, 1–16.

69 F. He, Y. Lu, Y. Wu, S. Wang, Y. Zhang, P. Dong, Y. Wang, C. Zhao, S. Wang, J. Zhang and S. Wang, *Adv. Mater.*, 2024, **36**, 2307490.

70 Y. Tang, X. Luo, R. Xia, J. Luo, S. Peng, Z. Liu, Q. Gao, M. Xie, R. Wei, G. Ning and D. Li, *Angew. Chem., Int. Ed.*, 2024, **63**, e202408186.

71 Y.-C. Hao, L.-W. Chen, J. Li, Y. Guo, X. Su, M. Shu, Q. Zhang, W.-Y. Gao, S. Li, Z.-L. Yu, L. Gu, X. Feng, A.-X. Yin, R. Si, Y.-W. Zhang, B. Wang and C.-H. Yan, *Nat. Commun.*, 2021, **12**, 2682.

72 J. Y. Choi, B. Check, X. Fang, S. Blum, H. T. B. Pham, K. Tayman and J. Park, *J. Am. Chem. Soc.*, 2024, **146**, 11319–11327.

73 Q. Liao, Q. Sun, H. Xu, Y. Wang, Y. Xu, Z. Li, J. Hu, D. Wang, H. Li and K. Xi, *Angew. Chem., Int. Ed.*, 2023, **62**, e202310556.

74 Q. Xue, H. Li, P. Jin, X. Zhou and F. Wang, *Angew. Chem., Int. Ed.*, 2025, **17**, 955.

75 C. Feng, J. Luo, C. Chen, S. Zuo, Y. Ren, Z. Wu, M. Hu, S. Ould-Chikh, J. Ruiz-Martinez, Y. Han and H. Zhang, *Energy Environ. Sci.*, 2024, **17**, 1520–1530.

76 X. Wu, J. van Waeyenberg, D. Vangestel and B. Sels, *Energy Environ. Sci.*, 2025, **18**, 1191–1204.